Full-range polarization-sensitive swept-source optical coherence tomography by simultaneous transversal and spectral modulation

Masahiro Yamanari, Shuichi Makita, Yiheng Lim, and Yoshiaki Yasuno

Computational Optics Group in the University of Tsukuba, Tsukuba, Ibaraki, Japan

yamanari@optlab2.bk.tsukuba.ac.jp

Abstract: Polarization-sensitive swept-source optical coherence tomography (PS-SS-OCT) is used to measure three-dimensional phase-retardation images of birefringent biological tissue *in vivo*. PS-SS-OCT with continuous source polarization modulation is used to multiplex the incident states of polarization in the signal frequency of each A-scan. Although it offers the advantage of measurement speed that is as high as that of standard SS-OCT, its disadvantage is low axial measurement range. To overcome this drawback, we employed the B-M-mode scan (BM-scan) method, which removes complex conjugate ambiguity by applying phase modulation along the transversal scanning direction. Since polarization modulation and BM-scan are applied in different scanning directions, these methods can be combined to make the optimum use of both full range and polarization-sensitive imaging. Phase fluctuations that cause measurement failure were numerically canceled before demodulating the B-scan oriented modulation. After removing complex conjugate artifacts, the axial measurement range was 5.35 mm, and the signal-to-conjugate ratio was 40.5 dB. We demonstrated retinal imaging using the PS-SS-OCT system with a frequency-swept laser at a center wavelength of 1064 nm and an axial resolution of 11.4 μm in tissue. Full-range polarization-sensitive retinal images showed characteristic birefringence of fibrous tissues such as retinal nerve fiber, sclera, and lamina cribrosa.

OCIS codes: (110.4500) Optical coherence tomography, (120.5410) Polarimetry, (170.4470) Ophthalmology.

References and links

1. M. R. Hee, D. Huang, E. A. Swanson, and J. G. Fujimoto, "Polarization-sensitive low-coherence reflectometer for birefringence characterization and ranging," J. Opt. Soc. Am. B **9**, 903–908 (1992).
2. J. F. de Boer, T. E. Milner, M. J. C. van Gemert, and J. S. Nelson, "Two-dimensional birefringence imaging in biological tissue by polarization-sensitive optical coherence tomography," Opt. Lett. **22**, 934–936 (1997).
3. B. Cense, T. C. Chen, B. H. Park, M. C. Pierce, and J. F. de Boer, "Thickness and birefringence of healthy retinal nerve fiber layer tissue measured with polarization-sensitive optical coherence tomography," Invest. Ophthalmol. Vis. Sci. **45**, 2606–2612 (2004).
4. M. Yamanari, M. Miura, S. Makita, T. Yatagai, and Y. Yasuno, "Phase retardation measurement of retinal nerve fiber layer by polarization-sensitive spectral-domain optical coherence tomography and scanning laser polarimetry," J. Biomed. Opt. **13**, 014013 (2008).

5. E. Götzinger, M. Pircher, B. Baumann, C. Hirn, C. Vass, and C. K. Hitzenberger, "Analysis of the origin of atypical scanning laser polarimetry patterns by polarization-sensitive optical coherence tomography," Invest. Ophthalmol. Vis. Sci. **49**, 5366–5372 (2008).
6. M. Pircher, E. Götzinger, O. Findl, S. Michels, W. Geitzenauer, C. Leydolt, U. Schmidt-Erfurth, and C. K. Hitzenberger, "Human macula investigated in vivo with polarization-sensitive optical coherence tomography," Invest. Ophthalmol. Vis. Sci. **47**, 5487–5494 (2006).
7. M. Miura, M. Yamanari, T. Iwasaki, A. E. Elsner, S. Makita, T. Yatagai, and Y. Yasuno, "Imaging polarimetry in age-related macular degeneration," Invest. Ophthalmol. Vis. Sci. **49**, 2661–2667 (2008).
8. C. Hitzenberger, E. Goetzinger, M. Sticker, M. Pircher, and A. Fercher, "Measurement and imaging of birefringence and optic axis orientation by phase resolved polarization sensitive optical coherence tomography," Opt. Express **9**, 780–790 (2001).
9. S. Jiao, M. Todorovic, G. Stoica, and L. V. Wang, "Fiber-based polarization-sensitive mueller matrix optical coherence tomography with continuous source polarization modulation," Appl. Opt. **44**, 5463–5467 (2005).
10. Y. Yasuno, S. Makita, Y. Sutoh, M. Itoh, and T. Yatagai, "Birefringence imaging of human skin by polarization-sensitive spectral interferometric optical coherence tomography," Opt. Lett. **27**, 1803–1805 (2002).
11. Y. Yasuno, S. Makita, T. Endo, M. Itoh, T. Yatagai, M. Takahashi, C. Katada, and M. Mutoh, "Polarization-sensitive complex Fourier domain optical coherence tomography for Jones matrix imaging of biological samples," Appl. Phys. Lett. **85**, 3023–3025 (2004).
12. B. Park, M. C. Pierce, B. Cense, S.-H. Yun, M. Mujat, G. Tearney, B. Bouma, and J. de Boer, "Real-time fiber-based multi-functional spectral-domain optical coherence tomography at 1.3 μm," Opt. Express **13**, 3931–3944 (2005).
13. E. Götzinger, M. Pircher, and C. K. Hitzenberger, "High speed spectral domain polarization sensitive optical coherence tomography of the human retina," Opt. Express **13**, 10217–10229 (2005).
14. M. Yamanari, S. Makita, V. D. Madjarova, T. Yatagai, and Y. Yasuno, "Fiber-based polarization-sensitive Fourier domain optical coherence tomography using b-scan-oriented polarization modulation method," Opt. Express **14**, 6502–6515 (2006).
15. W. Oh, S. Yun, B. Vakoc, M. Shishkov, A. Desjardins, B. Park, J. de Boer, G. Tearney, and B. Bouma, "High-speed polarization sensitive optical frequency domain imaging with frequency multiplexing," Opt. Express **16**, 1096–1103 (2008).
16. M. Yamanari, S. Makita, and Y. Yasuno, "Polarization-sensitive swept-source optical coherence tomography with continuous source polarization modulation," Opt. Express **16**, 5892–5906 (2008).
17. T. Schmoll, E. Götzinger, M. Pircher, C. K. Hitzenberger, and R. A. Leitgeb, "Single-camera polarization-sensitive spectral-domain oct by spatial frequency encoding," Opt. Lett. **35**, 241–243 (2010).
18. M. Yamanari, Y. Lim, S. Makita, and Y. Yasuno, "Visualization of phase retardation of deep posterior eye by polarization-sensitive swept-source optical coherence tomography with 1-μm probe," Opt. Express **17**, 12385–12396 (2009).
19. B. Považay, K. Bizheva, B. Hermann, A. Unterhuber, H. Sattmann, A. Fercher, W. Drexler, C. Schubert, P. Ahnelt, M. Mei, R. Holzwarth, W. Wadsworth, J. Knight, and P. S. J. Russell, "Enhanced visualization of choroidal vessels using ultrahigh resolution ophthalmic oct at 1050 nm," Opt. Express **11**, 1980–1986 (2003).
20. A. Unterhuber, B. Považay, B. Hermann, H. Sattmann, A. Chavez-Pirson, and W. Drexler, "In vivo retinal optical coherence tomography at 1040 nm - enhanced penetration into the choroid," Opt. Express **13**, 3252–3258 (2005).
21. E. C. Lee, J. F. de Boer, M. Mujat, H. Lim, and S. H. Yun, "In vivo optical frequency domain imaging of human retina and choroid," Opt. Express **14**, 4403–4411 (2006).
22. Y. Yasuno, Y. Hong, S. Makita, M. Yamanari, M. Akiba, M. Miura, and T. Yatagai, "In vivo high-contrast imaging of deep posterior eye by 1-um swept source optical coherence tomography and scattering optical coherence angiography," Opt. Express **15**, 6121–6139 (2007).
23. B. Považay, B. Hermann, A. Unterhuber, B. Hofer, H. Sattmann, F. Zeiler, J. E. Morgan, C. Falkner-Radler, C. Glittenberg, S. Blinder, and W. Drexler, "Three-dimensional optical coherence tomography at 1050 nm versus 800 nm in retinal pathologies: enhanced performance and choroidal penetration in cataract patients," J. Biomed. Opt. **12**, 041211–7 (2007).
24. V. J. Srinivasan, D. C. Adler, Y. Chen, I. Gorczynska, R. Huber, J. S. Duker, J. S. Schuman, and J. G. Fujimoto, "Ultrahigh-speed optical coherence tomography for three-dimensional and en face imaging of the retina and optic nerve head," Invest. Ophthalmol. Vis. Sci. **49**, 5103–5110 (2008).
25. P. Puvanathasan, P. Forbes, Z. Ren, D. Malchow, S. Boyd, and K. Bizheva, "High-speed, high-resolution Fourier-domain optical coherence tomography system for retinal imaging in the 1060 nm wavelength region," Opt. Lett. **33**, 2479–2481 (2008).
26. W. Y. Oh, S. H. Yun, G. J. Tearney, and B. E. Bouma, "115 khz tuning repetition rate ultrahigh-speed wavelength-swept semiconductor laser," Opt. Lett. **30**, 3159–3161 (2005).
27. R. Huber, D. C. Adler, and J. G. Fujimoto, "Buffered Fourier domain mode locking: unidirectional swept laser sources for optical coherence tomography imaging at 370,000 lines/s," Opt. Lett. **31**, 2975–2977 (2006).
28. M. Wojtkowski, A. Kowalczyk, R. Leitgeb, and A. F. Fercher, "Full range complex spectral optical coherence tomography technique in eye imaging," Opt. Lett. **27**, 1415–1417 (2002).

29. J. Zhang, W. Jung, J. Nelson, and Z. Chen, "Full range polarization-sensitive Fourier domain optical coherence tomography," Opt. Express **12**, 6033–6039 (2004).
30. A. M. Davis, M. A. Choma, and J. A. Izatt, "Heterodyne swept-source optical coherence tomography for complete complex conjugate ambiguity removal," J. Biomed. Opt. **10**, 064005 (2005).
31. M. Sarunic, M. A. Choma, C. Yang, and J. A. Izatt, "Instantaneous complex conjugate resolved spectral domain and swept-source oct using 3x3 fiber couplers," Opt. Express **13**, 957–967 (2005).
32. B. J. Vakoc, S. H. Yun, G. J. Tearney, and B. E. Bouma, "Elimination of depth degeneracy in optical frequency-domain imaging through polarization-based optical demodulation," Opt. Lett. **31**, 362–364 (2006).
33. B. Hofer, B. Považay, B. Hermann, A. Unterhuber, G. Matz, and W. Drexler, "Dispersion encoded full range frequency domain optical coherence tomography," Opt. Express **17**, 7–24 (2009).
34. B. Hofer, B. Považay, A. Unterhuber, L. Wang, B. Hermann, S. Rey, G. Matz, and W. Drexler, "Fast dispersion encoded full range optical coherence tomography for retinal imaging at 800 nm and 1060 nm," Opt. Express **18**, 4898–4919 (2010).
35. Y. Yasuno, S. Makita, T. Endo, G. Aoki, M. Itoh, and T. Yatagai, "Simultaneous b-m-mode scanning method for real-time full-range Fourier domain optical coherence tomography," Appl. Opt. **45**, 1861–1865 (2006).
36. R. K. Wang, "In vivo full range complex Fourier domain optical coherence tomography," Appl. Phys. Lett. **90**, 054103 (2007).
37. S. Vergnole, G. Lamouche, and M. L. Dufour, "Artifact removal in Fourier-domain optical coherence tomography with a piezoelectric fiber stretcher," Opt. Lett. **33**, 732–734 (2008).
38. C. Fan, Y. Wang, and R. K. Wang, "Spectral domain polarization sensitive optical coherence tomography achieved by single camera detection," Opt. Express **15**, 7950–7961 (2007).
39. L. An and R. K. Wang, "Use of a scanner to modulate spatial interferograms for in vivo full-range Fourier-domain optical coherence tomography," Opt. Lett. **32**, 3423–3425 (2007).
40. B. Baumann, M. Pircher, E. Götzinger, and C. K. Hitzenberger, "Full range complex spectral domain optical coherence tomography without additional phase shifters," Opt. Express **15**, 13375–13387 (2007).
41. R. A. Leitgeb, R. Michaely, T. Lasser, and S. C. Sekhar, "Complex ambiguity-free Fourier domain optical coherence tomography through transverse scanning," Opt. Lett. **32**, 3453–3455 (2007).
42. B. Vakoc, S. Yun, J. de Boer, G. Tearney, and B. Bouma, "Phase-resolved optical frequency domain imaging," Opt. Express **13**, 5483–5493 (2005).
43. S. Makita, T. Fabritius, and Y. Yasuno, "Full-range, high-speed, high-resolution 1μm spectral-domain optical coherence tomography using bm-scan for volumetric imaging of the human posterior eye," Opt. Express **16**, 8406–8420 (2008).
44. B. H. Park, M. C. Pierce, B. Cense, and J. F. de Boer, "Jones matrix analysis for a polarization-sensitive optical coherencetomography system using fiber-optic components," Opt. Lett. **29**, 2512–2514 (2004).
45. S. Makita, M. Yamanari, and Y. Yasuno, "Generalized Jones matrix optical coherence tomography: performance and local birefringence imaging," Opt. Express **18**, 854–876 (2010).
46. C. Brosseau, *Fundamentals of polarized light : a statistical optics approach* (John Wiley, 1998).

1. Introduction

Polarization-sensitive optical coherence tomography (PS-OCT) is a functional extension of OCT and it is used to measure depth-resolved birefringence of biological samples [1, 2]. It has been utilized to investigate distinctive birefringent tissues, e.g., retinal nerve fiber [3–5], retinal pigment epithelium [6], and fibrous tissue in age-related macular degeneration [7].

Early PS-OCT systems were implemented using the conventional time domain OCT [1, 2, 8, 9]. Recently, spectral domain (SD) OCT and swept-source (SS) OCT have been applied to PS-OCT to take advantage of its high sensitivity and high imaging speed [10–17]. We have demonstrated PS-SS-OCT with continuous polarization modulation at 1.3 μm for imaging anterior eye segment [16] and at 1 μm for retinal imaging [18]. The characteristic of our method is that all elements of the Jones matrix can be measured with a single depth scan. However, the tradeoff is the short axial measurement range, because optical frequency scanning by the light source and polarization modulation by the electrooptic modulator (EOM) are multiplexed to the signal frequency. For retinal imaging at 1 μm, the axial measurement range was limited to be 2.02 mm in tissue [18]. Because some diseased eyes have an elevated structure, a long axial measurement range is desired. In addition, OCT with a 1-μm probe beam is known to have high penetration to the choroid [19–25]. To obtain the full benefit of this high penetration, the long measurement range is also preferable to avoid OCT image overlapping accidentally with

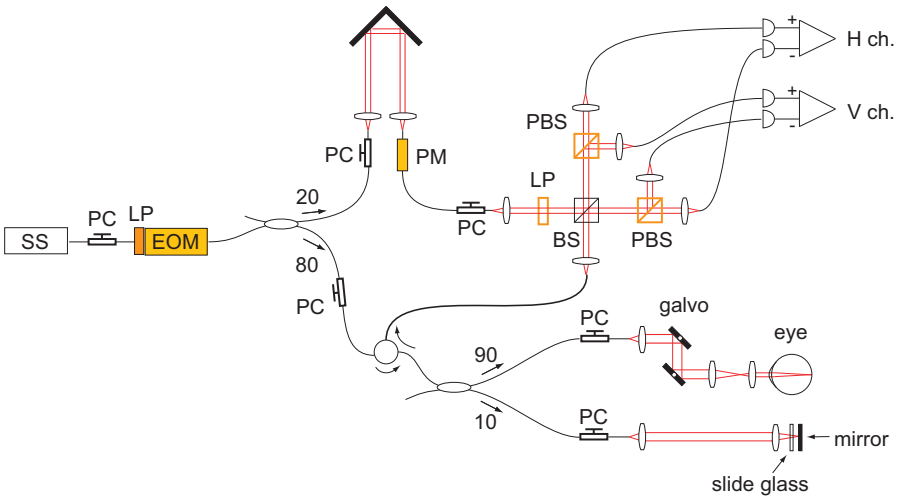

Fig. 1. Schematic diagram of system. SS: frequency-swept laser source, PC: polarization controller, LP: linear polarizer, EOM: electrooptic polarization modulator, PM: phase modulator, BS: beamsplitter, PBS: polarizing beamsplitter.

its mirror image, which can occur more frequently with the high-penetration OCT.

A straightforward way to overcome the problem of a short axial measurement range is to increase the digitizer sampling rate and the polarization modulation frequency. However, this requires expensive upgrades of high-speed photodetectors and digitizers. In addition, the requirements become more severe for ultra high-speed light sources [26, 27].

Another approach to improve the axial measurement range is full-range imaging. By removing complex conjugate artifacts in a Fourier-domain OCT, the axial measurement range can be doubled [28]. Several methods have been developed for this purpose. Complex conjugate artifacts have been removed instantaneously using a phase modulator [29], frequency shifter [30], 3×3 coupler [31], and a quadrature demodulator [32]. Numerical removal of complex conjugate artifacts has been demonstrated using dispersion encoding [33, 34]. Phase modulation along the B-scan, called BM-scan, is another way to remove complex conjugate artifacts [35, 36]. The BM-scan has also been implemented for SS-OCT [37] and PS-SD-OCT [38]. The transversal phase modulation of the BM-scan is applied by a phase modulator or transversal scanner [39–41]. The advantage of the BM-scan is that it does not require an additional detection channel and hardware for demodulation.

In this paper, we describe full-range PS-SS-OCT using polarization modulation and BM-scan. We show the configuration of the system in Section 2. Details of the algorithm are thoroughly explained in Section 3. We evaluate the performance of the system and demonstrate retinal imaging in Section 4, and the conclusion is presented in Section 5.

2. System

Figure 1 shows the schematic diagram of the full-range PS-SS-OCT system. The system is configured on the basis of our previously reported PS-SS-OCT system [18]. A major difference from the previous system is an additional phase modulator in the reference arm for the BM-scan.

The light source is a frequency swept laser (HSL-1000, Santec, Japan) with a center wavelength of 1064 nm, a wavelength range of 75 nm, a scanning rate of 30 kHz, and an average

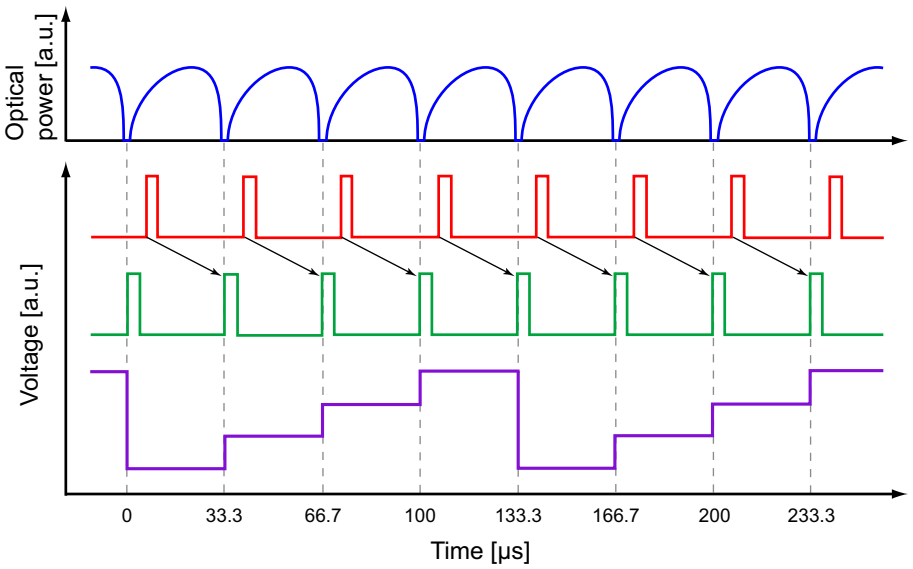

Fig. 2. Schematic of triggers and waveforms. Optical output power of light source (blue), trigger from light source (red), delayed trigger for the PM (green), and waveform driving PM (purple) are shown. The trigger from the light source is delayed to drive the PM, as indicated by black arrows.

output power of 8.7 mW. The axial resolution was measured to be 11.4 μm in tissue. The light is incident on an electrooptic polarization modulator (EOM) to sinusoidally modulate the incident state of polarization at a frequency of 40 MHz. The modulated light is divided by a 20/80 single-mode-fiber (SMF) coupler to the reference and sample arms. The reference light passes through a retroreflector and phase modulator (PM). The PM (NIR-MPX-LN-0.1-S-S-FA-FA, Photline Inc., France) applies sawtooth phase modulation with a step of $\pi/2$ for each A-scan. The trigger of the light source has a delay from the real starting time of optical frequency sweeping, as shown in Fig. 2, and therefore, the PM cannot be triggered directly. To synchronize the PM for the n-th A-scan, the trigger from the light source at the $(n-1)$-th A-scan is electrically delayed to be at the interval between the $(n-1)$ and n-th A-scans by a digital delay generator (9524, Quantum Composers, MT). In the sample arm, the light passes through a circulator and 10/90 coupler. The axis of the polarization mode dispersion of the circulator is aligned to be the same as the axis of the EOM. 10% of the light is used to illuminate a slide glass and a mirror to generate phase calibration signals, as explained in Section 3. We call this arm the calibration arm. The remaining 90% of the light from the circulator is used to illuminate a human eye through a two-axis galvanometer scanner. The beam spot on the galvo is aligned at the center of pivot to avoid a phase shift along the transversal scan. Backreflected light from the eye is coupled to a single-mode fiber and interferes with the reference light at the polarization-diversity detection arm. Horizontally and vertically polarized components of the interfered light are detected by balanced photodetectors. The electric signals are lowpass-filtered at 40 MHz, amplified, and acquired by a two-channel high-speed digitizer at 100 Msamples/s.

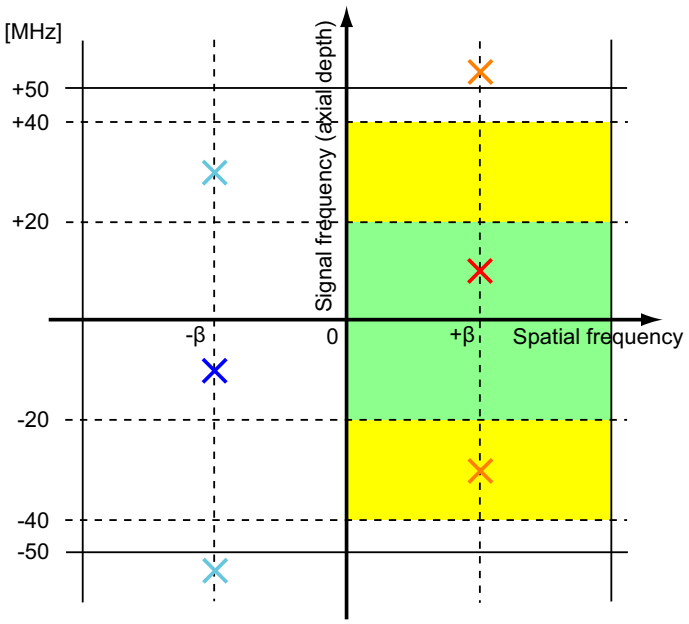

Fig. 3. Schematic figure of 2D Fourier transformed spectra. Red/blue and orange/light-blue crosses indicate central positions of complex conjugates of non-modulated and modulated signals, respectively. Green and yellow regions are extracted to obtain the non-modulated and modulated signals, respectively.

3. Method

3.1. Concept

Our full range PS-SS-OCT is a combination of polarization modulation and BM-scan [16, 35]. These modulations are applied to A-scans and B-scans, respectively. For intuitive understanding of the principle, we consider the two-dimensional Fourier transform of measured spectra corresponding to a B-scan, as shown in Fig. 3. Red/blue and orange/light-blue crosses indicate central positions of complex conjugates of non-polarization-modulated and polarization-modulated signals, respectively. In the vertical axis of the signal frequency for the A-scan, non-polarization-modulated and polarization-modulated OCT signals are separated. When complex conjugate artifacts are not removed, the available axial range is limited to half of the signal frequency space. Using the BM-scan, complex conjugate pairs are shifted to opposite directions in the spatial frequency space. By extracting the green and yellow regions shown in Fig. 3, polarization modulation is demultiplexed, and complex conjugate artifacts are removed. Note that half of the modulated signal range is extracted from the -1st-order signal, and the other half is extracted from the $+1$st-order signal to utilize the frequency range below the Nyquist frequency.

In practice, measured data cannot be directly demodulated as shown in Fig. 3 because there are several sources of phase fluctuation and systematic phase artifacts. To understand the phase property and cancel the fluctuation and artifacts, we begin with the mathematical formalization of the system.

3.2. *Interference of reference and sample beams*

Assuming that vertically polarized light passes through the EOM with its phase retardation of φ and fast axis oriented at $\pi/4$ radians with respect to the polarization state, the Jones vector of the light after the EOM is

$$\mathrm{J_R^{-1}}(\tfrac{\pi}{4}) \begin{bmatrix} e^{i\varphi/2} & 0 \\ 0 & e^{-i\varphi/2} \end{bmatrix} \mathrm{J_R}(\tfrac{\pi}{4}) \begin{bmatrix} 0 \\ 1 \end{bmatrix} = \begin{bmatrix} i\sin\varphi/2 \\ \cos\varphi/2 \end{bmatrix}, \tag{1}$$

where $\mathrm{J_R}(\theta)$ is a rotation matrix represented as

$$\mathrm{J_R}(\theta) = \begin{bmatrix} \cos\theta & \sin\theta \\ -\sin\theta & \cos\theta \end{bmatrix}, \tag{2}$$

$$\varphi = A_0 \sin(\omega_\mathrm{m} t - \phi(n)), \tag{3}$$

$A_0 = 2.405$ radians, ω_m is the angular frequency of the modulation, and $\phi(n)$ is the random phase offset of the modulation at the n-th A-scan.

The Jones matrix accounting for the birefringence of the sample and fiber-optic components after the EOM is defined as

$$\mathrm{J_{all}} = \mathrm{J_{out}} \mathrm{J_{sam}} \mathrm{J_{in}}, \tag{4}$$

where $\mathrm{J_{in}}$ is the Jones matrix between the EOM and the sample, $\mathrm{J_{sam}}$ is the double-pass Jones matrix of the sample, and $\mathrm{J_{out}}$ is the Jones matrix between the sample and detection arm. To simplify the equations discussed later, we rearrange Eq. (4) as

$$\mathrm{J_{all}} = \mathrm{J_{out}} \mathrm{J_{sam}} \mathrm{J_{in}} \mathrm{J_R^{-1}}(\tfrac{\pi}{4}) \mathrm{J_R}(\tfrac{\pi}{4}) \equiv \mathrm{J'_{all}} \mathrm{J_R}(\tfrac{\pi}{4}). \tag{5}$$

We set individual elements of $\mathrm{J'_{all}}$ as

$$\mathrm{J'_{all}} = \begin{bmatrix} j_{1,1} & j_{1,2} \\ j_{2,1} & j_{2,2} \end{bmatrix}. \tag{6}$$

Hereafter, we derive $\mathrm{J'_{all}}$ instead of $\mathrm{J_{all}}$. The Jones vector of the light from the sample at the detection arm is represented as

$$\begin{bmatrix} H_{sam} \\ V_{sam} \end{bmatrix} = \sqrt{P_s} s(k) \mathrm{J_{all}} \begin{bmatrix} i\sin\varphi/2 \\ \cos\varphi/2 \end{bmatrix} e^{i2kz_s} \tag{7}$$

$$= \frac{\sqrt{P_s} s(k)}{\sqrt{2}} \begin{bmatrix} j_{1,1} e^{i\frac{\varphi}{2}} + j_{1,2} e^{-i\frac{\varphi}{2}} \\ j_{2,1} e^{i\frac{\varphi}{2}} + j_{2,2} e^{-i\frac{\varphi}{2}} \end{bmatrix} e^{i2kz_s}, \tag{8}$$

where P_s, k, $s(k)$, and $2z_s$ are the proving power, wavenumber of the light, spectral density, and total double-path length of the sample arm, respectively. The wavenumber k depends on t as $k = k_0 + \alpha(t + \varepsilon(n))$, where k_0, α, t, and $\varepsilon(n)$ show the center wavenumber of the light source, scanning speed of the wavenumber, time, and fluctuation of the trigger at the n-th A-scan, respectively.

The polarization controller (PC) in the reference arm between the EOM and the PM is aligned so that the reference power is not modulated by the EOM. In this condition, a phase of the reference light is modulated by the EOM. The horizontally polarized component of the reference light is represented as

$$H_\mathrm{ref}(k) = \sqrt{P_r} s(k) e^{-i\frac{\varphi}{2}} e^{i\beta x} e^{i2kz_r}, \tag{9}$$

where P_r, β, x, and $2z_r$ are the reference power, spatial angular frequency applied by the PM, transversal position at the sample, and double-path length of the reference arm, respectively.

Depending on birefringence controlled by the PC, $e^{-i\frac{\varphi}{2}}$ in Eq. (9) can be replaced with $e^{+i\frac{\varphi}{2}}$. Because both cases provide a consistent result in the end, we consider only the case of Eq. (9). The horizontally polarized component of the interference signal is derived as

$$|H_{\mathrm{ref}}(k)+H_{\mathrm{sam}}(k)|^2 = |H_{\mathrm{ref}}(k)|^2+|H_{\mathrm{sam}}(k)|^2+H_{\mathrm{ref}}(k)H^*_{\mathrm{sam}}(k)+c.c. \tag{10}$$

$$= P_rS(k)+P_sS(k)+\frac{\sqrt{P_rP_s}S(k)}{\sqrt{2}}(j^*_{1,1}e^{-i\varphi}+j^*_{1,2})e^{i\beta x}e^{i2kz}+c.c., \tag{11}$$

where $S(k)=s^2(k)$ is the power spectral density of the light source, * indicates a complex conjugate, $z=z_r-z_s$, and $c.c.$ shows a complex conjugate of the third term. Equation (11) includes two modulations, namely, $e^{-i\varphi}$ of polarization modulation and $e^{i\beta x}$ of the BM-scan.

3.3. Demodulation of polarization modulation

To obtain a full-range OCT image, the two modulations should be demodulated. After detection and digitization of the interference signals, the polarization modulation is demodulated first. Using Bessel functions, the Fourier transform of $e^{-i\varphi}$ from time to angular frequency is rearranged as

$$\mathscr{F}_{t\omega}[e^{-i\varphi}] = J_0(A_0)-J_1(A_0)\left\{e^{-i\phi(n)}\delta(\omega-\omega_{\mathrm{m}})-e^{i\phi(n)}\delta(\omega+\omega_{\mathrm{m}})\right\}+(\text{higher orders}), \tag{12}$$

where $J_n(x)$ and $\delta(x)$ are the n-th order Bessel function of the first kind and Dirac delta function, respectively. Since $J_0(A_0)=0$ and the higher orders are filtered out by the electric lowpass filter, we consider only the $\pm$1st-order terms, i.e., the second term of Eq. (12). Using Eq. (12), the Fourier transform of the third term in Eq. (11) is rearranged as

$$\begin{aligned}&\mathscr{F}_{t\omega}\left[H_{\mathrm{ref}}(t)H^*_{\mathrm{sam}}(t)\right]\\ &=\left[-J_1(A_0)j^*_{1,1}\left\{e^{-i\phi(n)}\delta(\omega-\omega_{\mathrm{m}}-2\alpha z)-e^{i\phi(n)}\delta(\omega+\omega_{\mathrm{m}}-2\alpha z)\right\}+j^*_{1,2}\delta(\omega-2\alpha z)\right]\\ &\quad\times e^{i\beta x}e^{i2(k_0+\alpha\varepsilon)z},\end{aligned} \tag{13}$$

where we omit the coherence function and common factor $\sqrt{P_rP_s/2}$. Similarly, the fourth term becomes

$$\begin{aligned}&\mathscr{F}_{t\omega}\left[H^*_{\mathrm{ref}}(t)H_{\mathrm{sam}}(t)\right]\\ &=\left[+J_1(A_0)j_{1,1}\left\{e^{-i\phi(n)}\delta(\omega-\omega_{\mathrm{m}}+2\alpha z)-e^{i\phi(n)}\delta(\omega+\omega_{\mathrm{m}}+2\alpha z)\right\}+j_{1,2}\delta(\omega+2\alpha z)\right]\\ &\quad\times e^{-i\beta x}e^{-i2(k_0+\alpha\varepsilon)z}.\end{aligned} \tag{14}$$

Equations (13) and (14) indicate that $j_{1,1}$ and $j^*_{1,1}$ are shifted to $\pm\omega_{\mathrm{m}}$.

Figure 4 shows a diagram of the signal frequency and windows for demultiplexing. To demultiplex the signals, the non-modulated signal is extracted from -30 to $+30$ MHz. The modulated signal is extracted from -40 to -10 MHz and from $+10$ to $+40$ MHz. The regions that exceed the intermediate points between the non-modulated and modulated signals at ±20 MHz are margins for the broadened point spread function owing to the nonlinearity of the optical frequency scan and wavelength dispersion.

Since the electric circuit between the photodetectors and digitizer includes a high-order Butterworth lowpass filter, the measured signals have a frequency-dependent phase offset. It generates a depth-dependent phase offset between the non-modulated and modulated signals and results in artifacts of birefringence measurement. After demultiplexing of polarization modulation, we compensate for it numerically by using the frequency-dependent phase property of the lowpass filter, which is measured with a function generator as the signal source.

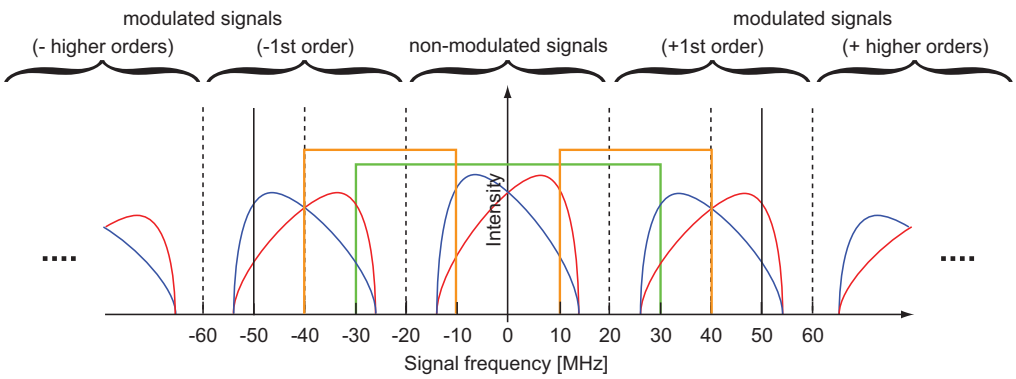

Fig. 4. Extracted regions of non-modulated (green) and modulated (orange) signals in signal frequency space. Red and blue curves are complex conjugates of each other. Note that the modulation and Nyquist frequencies of the sampling are 40 and 50 MHz, respectively.

Although the DC offset of spectra shown in the first and second terms of Eq. (11) is suppressed by balanced detection, it cannot be removed completely. To remove the residual DC offset, the averaged A-scan is subtracted from the non-modulated and modulated A-scans individually.

The A-scans are zero-padded, and the spectra are rescaled to compensate for the nonlinearity of the optical frequency scan by the light source. The group delay between the non-modulated and modulated signals attributed to polarization mode dispersion in the circulator is compensated for numerically by applying first-order dispersion to the spectra. Second-order dispersion between the reference and sample arms is also compensated for numerically. To increase the signal-to-conjugate ratio, second-order dispersion is intentionally induced by shortening the SMF (Corning HI1060) by 226 cm in the reference arm compared to the sample arm. Successive numerical dispersion compensation cancels this dispersion for the signal but doubles it for the conjugate and blurs the conjugate image. After multiplying a Gaussian window to the spectra, we calculate the Fourier transform of the spectra to obtain four complex OCT signals.

3.4. Compensation of phase fluctuation because of the trigger of light source

Before demodulating the BM-scan, phase fluctuation among A-scans must be compensated for. First, we consider large fluctuation of the trigger from the light source. According to the shift theorem of the Fourier transform, it generates a phase difference between A-scans that is in proportion to depth [42]. We measure it by using the front and back surfaces of the glass slide in the calibration arm. Assuming that the signals of the glass slide are well separated from their complex conjugate and any other signals of the sample, the non-modulated term $\tilde{I}_{h0}$, $+$ and -1st-order terms $\tilde{I}_{h(+1)}$, $\tilde{I}_{h(-1)}$ are described from Eq. (13) as

$$\tilde{I}_{h0} = j^*_{1,2} e^{i\beta x} e^{i2(k_0+\alpha\varepsilon)z} \tag{15}$$

$$\tilde{I}_{h(+1)} = -J_1(A_0) j^*_{1,1} e^{-i\phi(n)} e^{i\beta x} e^{i2(k_0+\alpha\varepsilon)z} \tag{16}$$

$$\tilde{I}_{h(-1)} = J_1(A_0) j^*_{1,1} e^{i\phi(n)} e^{i\beta x} e^{i2(k_0+\alpha\varepsilon)z}. \tag{17}$$

The phase difference between the first and n-th A-scans is derived using Eq. (15) as

$$\frac{\tilde{I}_{h0}(z,n)}{\tilde{I}_{h0}(z,0)} = e^{i2\alpha(\varepsilon(n)-\varepsilon(0))z} e^{i\beta(x(n)-x(0))}, \tag{18}$$

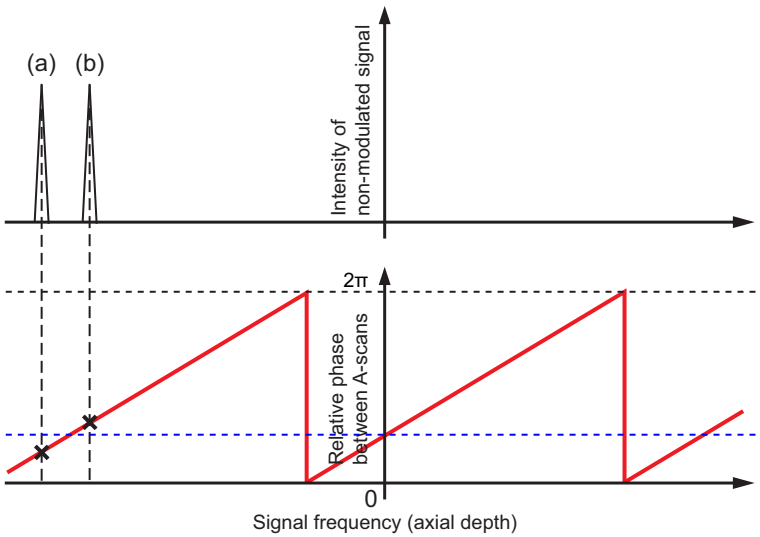

Fig. 5. Upper figure shows OCT intensity of non-modulated signal. (a) and (b) indicate the front and back surfaces of the slide glass. The lower figure shows the relative phase between the two A-scans. Red and blue lines show the estimated relative phase and the intercept.

where $\tilde{I}_{h0}(z,n)$ and $x(n)$ show the non-modulated term and lateral position at n-th A-scan, respectively. Since Eq. (18) shows that the phase difference depends on the axial position z linearly, it can be determined by the phase differences at two different depths, i.e., the front and back surfaces of the glass slide. Figure 5 shows a schematic of the depth-dependent phase difference between two A-scans. The slope is caused by the fluctuation of the trigger, and the intercept is caused by the BM-scan and mechanical vibration of the interferometer. If the distance between the front and back surfaces of the glass slide is too long, the relative phase between them exceeds 2π, and phase wrapping occurs, and consumes an axial range that is too large. If it is too short, the relative phase is too small to estimate the line accurately. The distance is determined as the intermediate between them. Using these signals, the slope and intercept of the phase shown in Eq. (18) are measured. When Eqs. (15), (16), and (17) are divided by Eq. (18), $\varepsilon(n)$ becomes a constant $\varepsilon(0)$ for all A-scans. Although the phase modulation by BM-scan is also canceled by this process, it is numerically retrieved later.

3.5. Compensation of phase fluctuation because of timing of polarization modulation

Since the EOM is not synchronized with the light source, it has a random phase offset $\phi(n)$ in Eq. (3). This generates phase fluctuation among A-scans of the modulated signals that is constant over the half-axial range. To cancel the fluctuation, we apply the same method as before [16]. The phase difference between the 0th and n-th A-scans is obtained by using non-modulated and modulated signals at the back surface of the slide glass as

$$\left(\frac{\tilde{I}_{h(+1)}(n)}{\tilde{I}_{h0}(n)}\right) \Big/ \left(\frac{\tilde{I}_{h(+1)}(0)}{\tilde{I}_{h0}(0)}\right) = e^{-i(\phi(n)-\phi(0))}. \tag{19}$$

After dividing Eq. (16) by Eq. (19) and multiplying Eq. (17) by Eq. (19), $\phi(n)$ becomes a constant $\phi(0)$ in Eqs. (16) and (17). Note that Eqs. (16) and (17) have a phase difference of $2\phi(0)$, as indicated in Fig. 6.

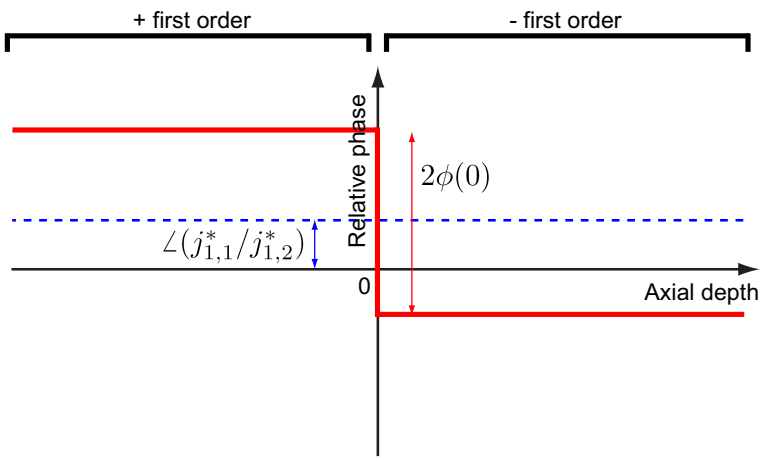

Fig. 6. Relative phase of OCT signals in full axial range. The red line shows $\angle(\tilde{I}_{h(-1)}/\tilde{I}_{h0})$ in the positive axial depth and $\angle(-\tilde{I}_{h(+1)}/\tilde{I}_{h0})$ in the negative axial depth. The blue dashed line shows their median, which equals $\angle(j_{1,1}^*/j_{1,2}^*)$.

3.6. *Demodulation of BM-scan*

The phase modulation $e^{i\beta x}$, which is canceled once by Eq. (18), is numerically recovered with *a priori* knowledge of the phase modulation by the PM. To demodulate the BM-scan, Eqs. (13) and (14) are Fourier transformed along the B-scan from the lateral position x to the spatial angular frequency ν as

$$\begin{aligned}
&\mathscr{F}_{x\nu}\mathscr{F}_{t\omega}[H_{\mathrm{ref}}(t)H_{\mathrm{sam}}^*(t)]\\
&=\Big[-J_1(A_0)j_{1,1}^*\left\{e^{-i\phi(0)}\delta(\omega-\omega_{\mathrm{m}}-2\alpha z,\nu-\beta)-e^{i\phi(0)}\delta(\omega+\omega_{\mathrm{m}}-2\alpha z,\nu-\beta)\right\}\\
&\quad+j_{1,2}^*\delta(\omega-2\alpha z,\nu-\beta)\Big]e^{i2(k_0+\alpha\varepsilon)z}
\end{aligned}\tag{20}$$

$$\begin{aligned}
&\mathscr{F}_{x\nu}\mathscr{F}_{t\omega}[H_{\mathrm{ref}}^*(t)H_{\mathrm{sam}}(t)]\\
&=\Big[+J_1(A_0)j_{1,1}\left\{e^{-i\phi(0)}\delta(\omega-\omega_{\mathrm{m}}+2\alpha z,\nu+\beta)-e^{i\phi(0)}\delta(\omega+\omega_{\mathrm{m}}+2\alpha z,\nu+\beta)\right\}\\
&\quad+j_{1,2}\delta(\omega+2\alpha z,\nu+\beta)\Big]e^{-i2(k_0+\alpha\varepsilon)z}.
\end{aligned}\tag{21}$$

As shown in Eqs. (20) and (21), the complex conjugates are separated as shown previously in Fig. 3. To remove the complex conjugate artifact, the positive spatial frequency is extracted using a window [43], shifted to zero spatial frequency, and inverse Fourier transformed to the original x domain.

3.7. *Compensation of phase difference between ±1st orders*

Since modulated signals have a phase difference $2\phi(0)$ between ±1st orders, as shown in Section 3.5, it must be compensated for to avoid the artifact in the birefringence calculation at the zero depth. To determine $2\phi(0)$, the signals of the glass slide, which is located in one side of the axial range, are not sufficient alone. An additional static mirror is placed in the calibration

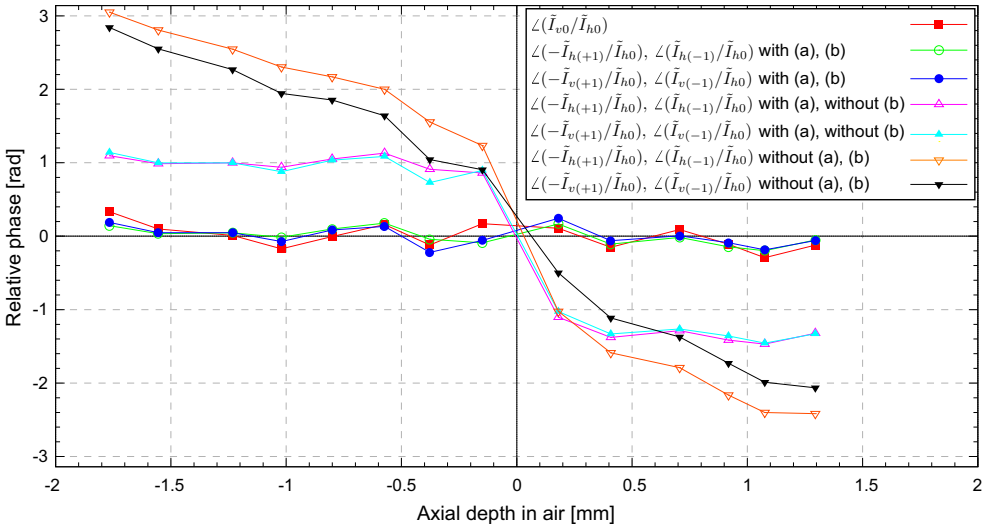

Fig. 7. Measured relative phases of OCT signals in full axial range. In the graph legends, (a) represents the phase compensation of the electric circuit and (b) represents the phase compensation estimated using Eq. (22). The relative phase averaged in the full axial depth was subtracted from each plot.

arm at the opposite side of the axial range to the zero delay point. The signals of the glass slide at z_{glass} and of the mirror at z_{mirror} can determine $2\phi(0)$ by using Eqs. (15)–(17) as

$$\left(\frac{\tilde{I}_{h(-1)}(z_{\mathrm{mirror}})}{\tilde{I}_{h0}(z_{\mathrm{mirror}})}\right) \Big/ \left(-\frac{\tilde{I}_{h(+1)}(z_{\mathrm{glass}})}{\tilde{I}_{h0}(z_{\mathrm{glass}})}\right) = e^{i2\phi(0)}. \tag{22}$$

Eqs. (16) and (17) are compensated for by the phase $\phi(0)$ determined by Eq. (22).

To confirm the phase compensation, the front and back surfaces of seven cover slips were measured as the sample. Figure 7 shows the measured relative phases with and without phase compensation of the electric circuit as described in Section 3.3 and the phase compensation of Eq. (22). The signal phases are normalized by $\tilde{I}_{h0}$ at each axial position to cancel the depth-dependent phase term. Without both of the phase compensations, the relative phases have depth dependence and an abrupt change at the zero depth. With phase compensation of the electric circuit, the depth-dependent artifact is removed except for the zero depth. With both phase compensations, the relative phases have no artifact over the full axial range.

To remove fixed pattern noise because of ghost signals in the calibration arm, OCT signals are averaged in each B-scan and subtracted from each A-scan.

3.8. Eigenvalues and eigenvectors of measured Jones matrix

After demodulation of the BM-scan, Eqs. (15)–(17) are free from complex conjugate ambiguity. By applying the same algorithm for vertically polarized component of the interference, non-modulated $\tilde{I}_{v0}$, $+1$st-order modulated $\tilde{I}_{v(+1)}$, and -1st-order modulated $\tilde{I}_{v(-1)}$ are calculated. We then obtain the measured Jones matrix as

$$\begin{bmatrix} -\tilde{I}^*_{h(+1)} & \tilde{I}^*_{h0} \\ -\tilde{I}^*_{v(+1)} & \tilde{I}^*_{v0} \end{bmatrix} = \begin{bmatrix} \tilde{I}^*_{h(-1)} & \tilde{I}^*_{h0} \\ \tilde{I}^*_{v(-1)} & \tilde{I}^*_{v0} \end{bmatrix} = e^{-2i(k_0+\alpha\varepsilon(0))z} \mathrm{J}'_{\mathrm{all}}. \tag{23}$$

The measured Jones matrices at the surface of the sample are normalized by $\angle\tilde{I}_{h0}$ for each A-scan to cancel the depth-dependent phase and are averaged in each B-scan. The inverse matrix is multiplied by Eq. (23) to rearrange the matrix as unitary or similar transformation of J_{sam} [44, 45]. We denote this rearranged matrix as [a, b; c, d]. Since $J_R(\frac{\pi}{4})$ is canceled by this process, the algorithm works using J'_{all} instead of J_{all} without any difference. Eigenvalues λ_1, λ_2 of the matrix are calculated using the equations for a 2×2 matrix as

$$\lambda_1 = \frac{T}{2} + \sqrt{\frac{T^2}{4-D}} \tag{24}$$

$$\lambda_2 = \frac{T}{2} - \sqrt{\frac{T^2}{4-D}}, \tag{25}$$

where T and D are the trace and determinant of [a, b; c, d], respectively. The eigenvectors are calculated as

$$\begin{bmatrix} \lambda_1 - d \\ b \end{bmatrix}, \begin{bmatrix} \lambda_2 - d \\ b \end{bmatrix}. \tag{26}$$

Phase retardation, diattenuation, and relative orientation of the sample are calculated from Eqs. (24)–(26) [46].

4. Results and discussions

4.1. Performance of full range measurement

Figure 8 shows the averaged A-scan profiles before and after the demodulation of BM-scan. The signals of the slide glass and the static mirror in the calibration arm were located on the both sides of the full axial range. The available axial measurement range was also limited by these signals in the calibration arm. After removing the complex conjugate artifact, the axial measurement range was 5.35 mm in air or 3.88 mm in tissue, assuming a refractive index of 1.38. For half-range imaging without the BM-scan, compensation for only the phase fluctuation because of the timing of polarization modulation shown in Eq. (19) is sufficient to apply averaging of the surface Jones matrices. In this case, only the single signal shown in Fig. 8 (a) is required, and the axial measurement range was 3.52 mm in air or 2.55 mm in tissue. This measurement range is not sufficiently wide for measuring some clinical cases including an optic nerve head with deep cupping and retinal diseases with high elevation. The extended axial measurement range with a BM-scan was 1.52 times longer than the case without a BM-scan.

In Fig. 8, a static mirror was placed near the zero depth as a sample. The measured signal-to-conjugate ratio, i.e., (c) to (d) in Fig. 8, was 40.5 dB. Both of the numerical compensation of the second-order dispersion and demodulation of the BM-scan contributed to the signal-to-conjugate ratio. The sensitivity of the system was measured to be 97.7 dB near the zero depth, and the signal roll-off was measured to be -1.9 dB/mm in air or -2.6 dB/mm in tissue for both directions from the central zero depth.

These results showed that BM-scan method was successfully applied to this system.

4.2. Retinal imaging

To demonstrate full-range PS-SS-OCT imaging, retinal imaging was performed on a human volunteer after informed consent was obtained. This *in vivo* measurement was approved by the Institutional Review Board of the University of Tsukuba and conformed to the Declaration of Helsinki. Figures 9(a) and (b) show the intensity images of the optic nerve head before and after removing the complex conjugate artifact, respectively. Before removal, the DC and complex conjugate obscured the real structure. After removal, the retinal structure could be visualized.

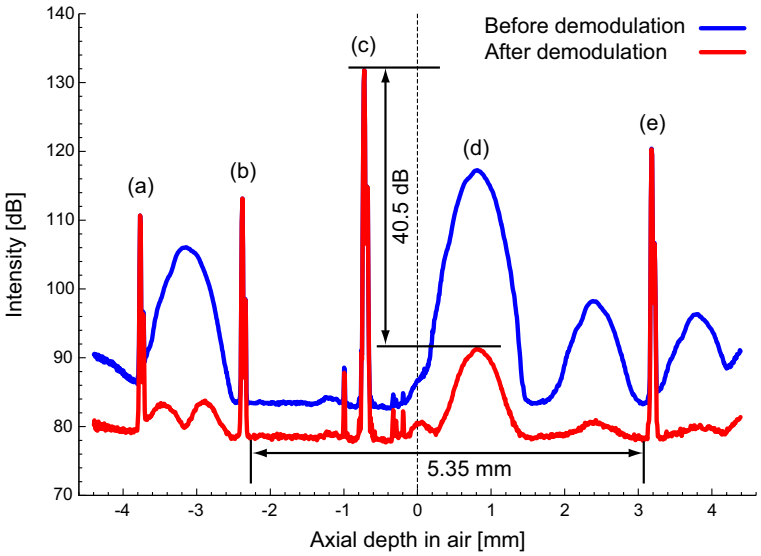

Fig. 8. Averaged A-scan profiles before (blue) and after (red) demodulation of BM-scan. (a) and (b) indicate the front and back surfaces of the slide glass in the calibration arm. (c) and (d) indicate the mirror and its complex conjugate signal in the sample arm. (e) indicates the mirror in the calibration arm.

The green arrows indicate residual artifacts caused by flow in large blood vessels. Figure 9(c) shows the phase retardation image before removing the complex conjugate artifact, which obscured the real signals. After removing the complex conjugate artifact, phase retardation images of Figs. 9(d) and (e) were obtained. They show the phase retardation images before and after the phase compensation described in Section 3.7, respectively. An artifact of the abrupt change in phase retardation was observed at the zero depth, as indicated by the white arrow in Fig. 9(d). After the compensation, this artifact at the zero depth was removed, and the phase retardation image of lamina cribrosa was correctly visualized, as shown in Fig. 9(e). This demonstrates the importance of phase compensation in our system.

Figure 10 shows B-scan images of the retina between the macula and optic nerve head (ONH) of the myopic right eye. The sclera is visible in the intensity image because of high penetration at a 1 μm wavelength. The scleral birefringence was higher at the peripheral region. The myopic conus, which is sclera exposed at the periphery of ONH, was found in the intensity image and is indicated with a red arrow. In the phase retardation image, it changed the phase retardation over π radians, indicating strong birefringence at this region. Figures 10(c) and (d) show the intensity and phase retardation images at a superior region to Figs. 10(a) and (b), respectively. In this region, the phase retardation was changed by thick retinal nerve fiber. Beneath it, sclera also changed the phase retardation. Figure 11 shows the close-up measurement of the ONH for the myopic left eye. Lamina cribrosa in the ONH showed characteristic changes of phase retardation. *En face* slices of the intensity and phase retardation volumes are shown in the movie of Fig. 12. The intensity images show individual pores of the lamina cribrosa. The phase retardation was higher at the nasal and temporal regions than at the superior and inferior regions of the lamina cribrosa. This inhomogeneity may imply that the microstructure of the lamina cribrosa is not homogeneous in the ONH. These results demonstrate that full-range PS-SS-OCT can measure a healthy retina with wide range and high penetration; thus, it is suitable for measuring diseased eyes, which often have large deformations.

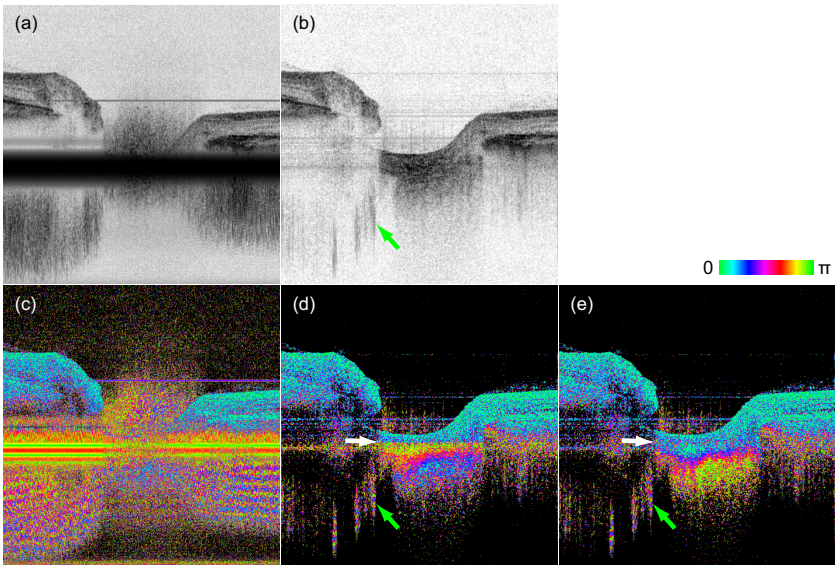

Fig. 9. Intensity images (a) before and (b) after demodulation of BM-scan, and phase retardation images (c) before and (d), (e) after demodulation of BM-scan. (d) and (e) are the phase retardation images before and after compensation of phase difference estimated using Eq. (22), respectively. The subject was the optic nerve head of the left eye of the human volunteer. 1024 A-scans and 94 B-scans were acquired in 34.1 ms and 3.8 s, respectively. The image size is 2.7 (x) $\times$ 2.73 (z) mm^2. In (c)–(e), low-intensity regions are masked by black color. Intensity movies (Media 1, Media 2) and phase-retardation movies (Media 3, Media 4) are available.

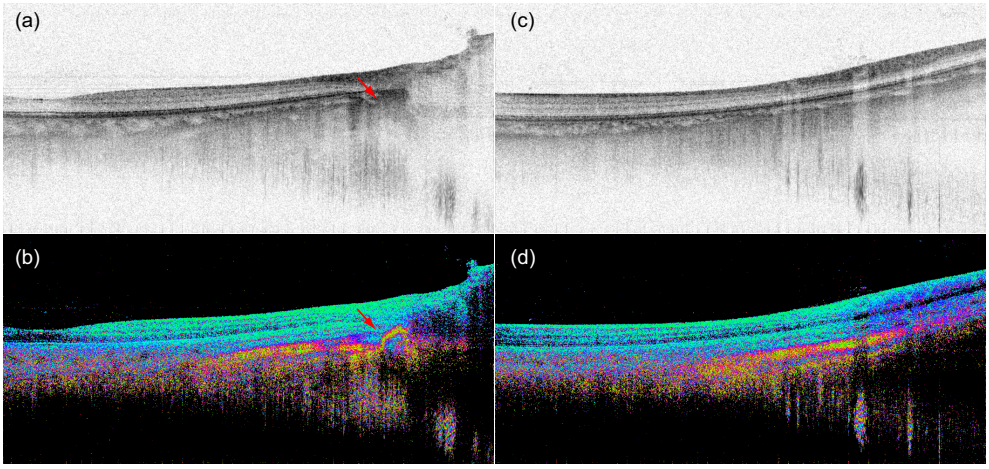

Fig. 10. (a) Intensity and (b) phase retardation images of retina between fovea and ONH. (c) and (d) are intensity and phase retardation images at superior region, respectively. Red arrows indicate a myopic conus. 2048 A-scans were acquired in 68.3 ms. The image size is 6.0 (x) $\times$ 2.79 (z) mm^2.

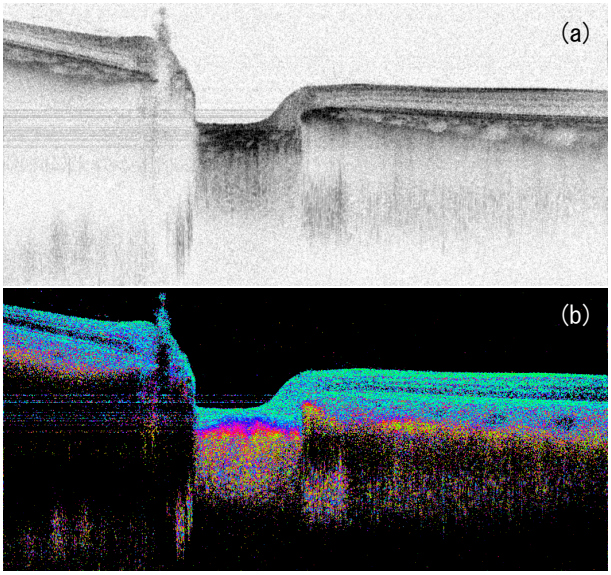

Fig. 11. (a) Intensity and (b) phase retardation images of ONH. 2048 A-scans were acquired in 68.3 ms. The image size is 6.0 (x) $\times$ 2.79 (z) mm^2.

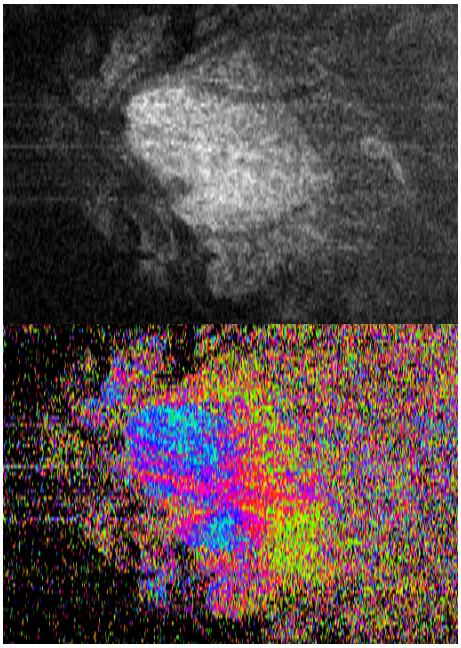

Fig. 12. (upper) *en face* intensity and (lower) phase retardation images of optic nerve head. The movies show the *en face* slices from the anterior to the posterior direction (Media 5, Media 6). 1024 A-scans and 94 B-scans were acquired in 34.1 ms and 3.8 s, respectively. The image size is 2.7 $\times$ 1.9 mm^2.

5. Conclusion

In conclusion, we demonstrated high-penetration imaging for the sclera and lamina cribrosa of healthy human eyes and found the BM-scan method effective for full-range imaging in PS-SS-OCT. With a signal-to-conjugate ratio of 40.5 dB, complex conjugate artifacts were significantly diminished in the retinal images and the axial measurement range was extended to 3.88 mm from 2.55 mm. The full range and high penetration would be helpful for examining patients with a wide spectrum of diseases.

Acknowledgements

We are grateful to Barry Cense for helpful comments to improve the expressions. This research was supported in part by the Japan Science and Technology Agency through the program of Development of Systems and Technology for Advanced Measurement and Analysis.